Hindawi
Shock and Vibration
Volume 2023, Article ID 8374444, 19 pages
https://doi.org/10.1155/2023/8374444

Research Article

Bursting Oscillation Mechanisms of a Desktop Medical Shaker with Eccentric Turntables Affected by Dry Friction

Rui Qu [1] **and Xin Xia** [2]

[1]*Faculty of Civil Engineering and Mechanics, Jiangsu University, Zhenjiang 212013, China*
[2]*School of Medicine, Jiangsu University, Zhenjiang 212013, China*

Correspondence should be addressed to Rui Qu; 2111623003@stmail.ujs.edu.cn and Xin Xia; 1000005066@ujs.edu.cn

Received 7 August 2023; Revised 15 November 2023; Accepted 28 November 2023; Published 13 December 2023

Academic Editor: Yan Niu

The main purpose of this article is to investigate the bursting oscillations of the medical shaking tables resulted from friction in practical application. Using the theoretical method of linear loading, the analytic expression of friction acting on an eccentric turntable is derived in detail. Besides, through numerical simulation, the decisive role of friction in bursting oscillations is verified. On this basis, several practical operation plans are proposed to eliminate harmful vibrations. Last but not least, the effectiveness of theoretical methods is validated through example calculations in cases with special parameters.

1. Introduction

Due to the low cost and high stability, desktop shakers with eccentric turntables [1–3] are widely used in the sample preparation process of medical experiments. The oscillator of the desktop shaker and the turntable are connected through the eccentric shaft [4, 5], forming a typical nonlinear, multiple-scale, and strongly coupled system with complicated dynamic behaviors. Many valuable studies [6–8] have been conducted on the application of eccentric shafts in existing literature, but this does not mean that the eccentric shaft is perfect. Actually, in its practical applications, the mechanical failure [9–11] has widely found that the actual speed of a desktop shaker intermittently exceeds the set speed after prolonged use, which corresponds to busting oscillations [12–14] in the rotor-oscillator system and can be named overspeed oscillation. Different from other current research work focusing on the application of eccentric shaft technology, the main task of this paper is to study defects, causes, and solutions of it.

In order to solve this typical medical device failure problem, the analytical expression of the friction between the eccentric turntable and adjacent components is bound to be derived, which is rarely reported in the existing research studies. On this basis, we should also investigate how the friction acting on eccentric turntables interferes with the dynamic behavior of the oscillator and propose the effective method to eliminate the harmful vibration.

In this paper, the analytical expression of friction between the turntable with eccentric shaft and the oscillator is derived in detail by means of simplification of linear load [10]. The maximum value of eccentricity and radius of turntable directly determine the integral interval, which needs to be discussed separately. The mathematical model of the rotor-oscillator system [15–17] is constructed based on the acceleration synthesis theorem when the embroil motion is translation. Meanwhile, the equilibrium curves and transformed phase portraits [18, 19] are used to investigate the mechanism of bifurcation and bursting oscillation. Based on these theoretical mechanisms and their corresponding physical significance, three feasible methods to eliminate or avoid the overspeed oscillation are proposed. Finally, the analytic solution of the friction in the case with a special parameter is obtained by geometric analysis to verify the validation of the theoretical method employed.

2. Derivation of the Analytic Expression of the Friction

The physical photo and structural sketch of a desktop medical shaker with eccentric turntables are shown in Figure 1. Sliding friction exists between the turntable and its neighboring members in a rotor-oscillator system.

The solution of this type of friction can be simplified to the following theoretical problem shown in Figure 2. A thin homogeneous disc of mass m is placed flat on a table (the plane where the screen is located) and is subjected to sliding friction when it is rotated around a point O on a fixed axis. The coefficient of kinetic friction between the table and the disk is μ. Try to calculate the friction force between the disc and horizontal table.

Take the small red triangle ΔOAB with vertex angle $d\theta$ as the area microelement and further mesh this area microelement along the normal direction of OA. Notice that the frictional force on all the meshes of the area microelement is in the same direction perpendicular to OA and the magnitude is proportional to the area of each mesh. All grids can be approximated as rectangles with equal dimensions along the OA direction, while the dimensions along the OA normal direction are proportional to the distance of that grid to the point of the axis of rotation O. Therefore, the grid area is linearly distributed along the OA direction, and thus, the distribution of the magnitude of the sliding friction force on each grid along the OA direction can be considered as a linear load. Based on the simplification method of a planar arbitrary force system, this linear load can be reduced to a concentrated force as shown in Figure 3.

Since there are many mathematical symbols involved in the derivation process, we sort out the physical meaning of each involved mathematical symbol as shown in Table 1.

Step 1: Determine the size of the main vector.

The magnitude of the microforce acting on a microspan of dx shown in can be expressed as follows:

$$dF = q(x)dx, \tag{1}$$

where $q(x)$ denotes the load set degree function at that place, and its expression can be expressed according to the linear relationship as follows:

$$\frac{x}{L} = \frac{q(x)}{q} \Longrightarrow q(x) = \frac{q}{L}x, \tag{2}$$

where L represents the total distribution length of linear load while q describes the maximum load set degree. Summing all force differential elements, the magnitude of the principal vector F is obtained as follows:

$$F = \int dF = \int_0^L \frac{q}{L}x dx = \frac{1}{2}qL. \tag{3}$$

Step 2: Determine the acting point of the combined force.

From the combined moment theorem, the moment of the combined force on the point O is equal to the sum of the moments of the component forces on the point O. The mathematical expression of this conclusion is as follows:

$$Fx = \int_0^L x \cdot dF = \int_0^L \frac{q}{L}x^2 dx = \frac{q}{3L}x^3\Big|_0^L = \frac{1}{3}qL^2. \tag{4}$$

Therefore,

$$x = \frac{(1/3)qL^2}{(1/2)qL} = \frac{2}{3}L. \tag{5}$$

Step 3: Derive the expression for the maximum load set degree.

In order to apply this result, we also need to derive the expression for the maximum load set degree q. According to the definition of the load set degree at a point, there is the following equation:

$$q(x) = \frac{\mathrm{d}F}{\mathrm{d}x}, \tag{6}$$

and the relationship between the force microelement dF and the grid area dS is as follows:

$$\mathrm{d}F = \mathrm{d}S \cdot \sigma, \tag{7}$$

where the surface density $\sigma = mg\mu/\pi r^2$ indicates the frictional force per unit area.

Substituting the expression for the area of the rectangular grid $dS = dx \cdot (x \cdot d\theta)$ into formula (7), one may obtain the expression for the load set degree function as follows:

$$dF = (x \cdot \sigma \cdot d\theta) \cdot dx \Longrightarrow q(x)\frac{dF}{dx} = x\sigma d\theta \propto x, \tag{8}$$

where $d\theta$ represents the vertex angle of the microarea ΔOAB. Notice that $q(x)$ is proportional to x. This further verifies the conjecture that the friction force is linearly distributed over the area microarea ΔOAB. On this basis, the maximum load set can be found as follows:

$$q = q(L) = L\sigma d\theta. \tag{9}$$

Note that the eccentric shaft may not be located inside the disc but may also be located outside the disc, which needs to be discussed separately.

2.1. Case 1: $a < r$

2.1.1. Main Vector. According to the calculation of the equivalent concentrated force of the linear load, the friction force on the area microelement can be expressed as follows:

$$df = \frac{1}{2}qL = \frac{\sigma}{2}L^2(\theta)d\theta. \tag{10}$$

According to the left-right symmetry of the disc, all components of sliding friction in the vertical direction cancel each other, i.e., $f_y = 0$. The horizontal component of

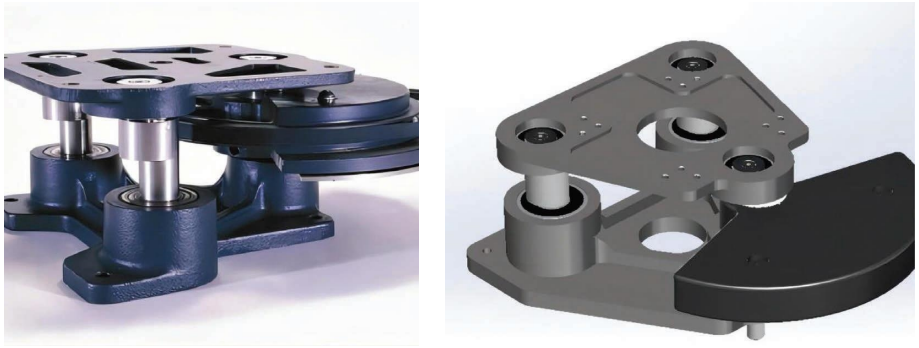

(a) (b)

Figure 1: (a) Physical photo and (b) structural sketch of the desktop medical shaker with eccentric turntables.

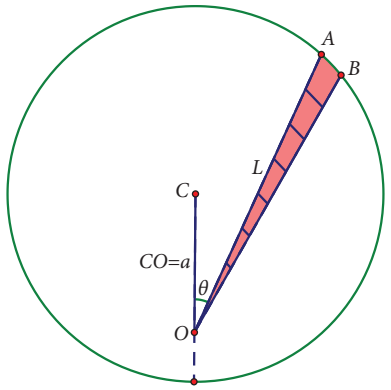

Figure 2: Schematic representation of a simplified model of friction.

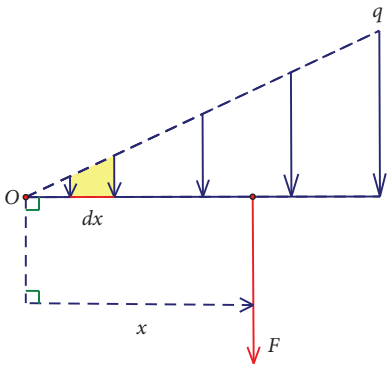

Figure 3: Equivalent concentrated force for linear loads.

Table 1: Physical significance of each mathematical symbol related to the linear loads.

Mathematical symbol	Physical meaning
dx	Length of a microspan
dF	Magnitude of the microforce acting on a microspan
$q(x)$	Load set degree function
q	The maximum load set degree
L	Total distribution length of linear load
F	Principal vector of equivalent concentrated force
σ	Frictional force per unit area
dS	Area of the rectangular grid
$d\theta$	Vertex angle of the microarea

sliding friction to which the area microelement is subjected can be expressed as follows:

$$df_x = \frac{1}{2}qL\cos\theta = \frac{\sigma}{2}L^2(\theta)\cos\theta d\theta. \tag{11}$$

According to the cosine theorem in triangle OCA, the following equivalence relation can be obtained:

$$\cos\theta = \frac{a^2 + L^2 - r^2}{2aL}. \tag{12}$$

The expression of the length of OA = L can be obtained through its geometric relationship between the eccentricity CO = a and radius r as follows:

$$L = a\cos\theta + \sqrt{r^2 - a^2\sin^2\theta}. \tag{13}$$

Therefore, the value of the friction can be expressed in the form of a definite integral as follows:

$$f_x = \frac{\sigma}{2}\int_0^{2\pi} L^2(\theta)\cos\theta d\theta, \tag{14}$$

where

$$\int_0^{2\pi} L^2(\theta)\cos\theta d\theta = \int_0^{2\pi}\left[a^2\cos^3\theta + 2a\cos^2\theta\sqrt{r^2 - a^2\sin^2\theta} + r^2\cos\theta - a^2\cos\theta\sin^2\theta\right]d\theta. \tag{15}$$

Note that the definite integral of the first, third, and fourth terms in the integral range is exactly zero.

$$0 = \int_0^{2\pi}\cos^3\theta d\theta = \int_0^{2\pi}\cos\theta d\theta = \int_0^{2\pi}\cos\theta\sin^2\theta d\theta. \tag{16}$$

Therefore,

$$f_x = \frac{\sigma}{2}\int_0^{2\pi} L^2(\theta)\cos\theta d\theta = \sigma a\cdot\int_0^{2\pi}\cos^2\theta\sqrt{r^2 - a^2\sin^2\theta}d\theta. \tag{17}$$

It is not difficult to find that the integral results in an elliptic integral, indicating that there is no analytic expression of elementary function. However, the analytic solution exists in the special case $a = r$ with $L = r(\cos\theta + |\cos\theta|) \Longrightarrow L^2\cos\theta = 2r\cos^3\theta + 2r\cos^2\theta|\cos\theta|$.

$$\begin{aligned} f_x &= \sigma a\cdot\int_0^{2\pi}\cos^2\theta\sqrt{r^2 - a^2\sin^2\theta}d\theta \\ &= \sigma r^2\cdot\int_0^{2\pi}\cos^2\theta|\cos\theta|d\theta \\ &= 4\sigma r^2\cdot\int_0^{(\pi/2)}\cos^3\theta d\theta \\ &= 4\sigma r^2\cdot\int_0^1\left[1 - \sin^2\theta\right]d(\sin\theta) \\ &\overset{t=\sin\theta}{=} 4\sigma r^2\int_0^1\left[1 - t^2\right]dt \\ &= 4\sigma r^2\cdot\left[t - \frac{t^3}{3}\right]\Big|_0^1 \\ &= \frac{8}{3\pi}mg\mu < mg\mu. \end{aligned} \tag{18}$$

It should be noted that the calculation result of this case must be less than that of $a = \infty$. The physical significance is as follows: when the eccentric shaft is located at infinity, the disc makes an instantaneous translation and the value of the friction is exactly $mg\mu$.

2.1.2. Principal Moment. Applying the simplified result of the linear load, the micromoment of equivalent concentrated force on the eccentric shaft can be found as follows:

$$dM = dF\cdot\frac{2}{3}L = \frac{1}{3}qL^2 = \frac{1}{3}(L\sigma d\theta)\cdot L^2 = \frac{\sigma}{3}L^3 d\theta. \tag{19}$$

Integrating the moment differential, the principal moment M of the friction on the simplified center O can be obtained as follows:

$$M = \frac{\sigma}{3}\int_0^{2\pi} L^3(\theta)d\theta. \tag{20}$$

From the cosine theorem, the expression of L^3 in the integral sign can be derived as follows:

$$L^2 - 2aL\cos\theta + a^2 - r^2 = 0 \Longrightarrow L^3 = 2aL^2\cos\theta + L\left(r^2 - a^2\right). \tag{21}$$

In equation (21), the integral of the first term $2aL^2\cos\theta$ has been calculated during the derivation of the main vector (18), while $r^2 - a^2$ is constant in the second term, so only the integral of L needs to be calculated as follows:

$$\begin{aligned} \int_0^{2\pi} L(\theta)d\theta &= \int_0^{2\pi} a\cos\theta + \sqrt{r^2 - a^2\sin^2\theta}d\theta \\ &= \int_0^{2\pi}\sqrt{r^2 - a^2\sin^2\theta}d\theta. \end{aligned} \tag{22}$$

The integral is still an elliptic integral with no analytic expression of elementary function, but in the special case $a = r$, there exists an analytic expression:

$$
\begin{aligned}
M &= \frac{\sigma}{3}\int_0^{2\pi} 2rL^2\cos\theta d\theta \\
&= \frac{2\sigma r}{3}\int_0^{2\pi} L^2\cos\theta d\theta \\
&= \frac{2\sigma r}{3}\int_0^{2\pi} 2r^2\cos^2\theta|\cos\theta|d\theta \\
&= \frac{16\sigma r^3}{3}\int_0^{\frac{\pi}{2}} \cos^3\theta d\theta \\
&= \frac{16mg\mu r}{3\pi}\cdot\frac{2}{3} = \frac{32mg\mu r}{9\pi}.
\end{aligned}
\tag{23}
$$

The distance D from the acting point of the combined friction force to the eccentric shaft is equal to the ratio of the principal moment to main vector.

$$
\begin{aligned}
D &= \frac{M}{f_x} = \frac{(\sigma/3)\int_0^{2\pi} L^3(\theta)d\theta}{\sigma a\int_0^{2\pi}\cos^2\theta\sqrt{r^2-a^2\sin^2\theta}} = \frac{(\sigma/3)\int_0^{2\pi} 2aL^2\cos\theta + \left(r^2-a^2\right)Ld\theta}{\sigma a\int_0^{2\pi}\cos^2\theta\sqrt{r^2-a^2\sin^2\theta}} \\
&= \frac{\left(4\sigma a^2/3\right)\int_0^{2\pi}\cos^2\theta\sqrt{r^2-a^2\sin^2\theta}d\theta + \left(\sigma\left(r^2-a^2\right)/3\right)\int_0^{2\pi} Ld\theta}{\sigma a\int_0^{2\pi}\cos^2\theta\sqrt{r^2-a^2\sin^2\theta}d\theta} \\
&= \frac{4a}{3} + \frac{r^2-a^2}{3a}\cdot\frac{\int_0^{2\pi}\sqrt{r^2-a^2\sin^2\theta}d\theta}{\int_0^{2\pi}\cos^2\theta\sqrt{r^2-a^2\sin^2\theta}d\theta} \\
&> \frac{4a}{3} + \frac{r^2-a^2}{3a} = \frac{r^2}{3a} + a.
\end{aligned}
\tag{24}
$$

In particular, when $a = r$,

$$
D = \frac{M}{f_x} = \frac{(32mg\mu r/9\pi)}{(8mg\mu/3\pi)} = \frac{4}{3}r. \tag{25}
$$

2.2. Case 2: $a > r$. We can still try to handle this case using the equivalent concentrated force of the linear load shown in Figure 4. Adding several pairs of equal and opposite sets of forces to the line OE makes the forces represented in blue a complete set of linear loads. In this case, the red part also constitutes a linear load with the opposite direction to the blue part. The lengths of the line segments OA and OE as well as the maximum load set degree on them can be easily expressed as through geometrical relationships.

Based on the geometrical relationships as shown in Figure 5, the following geometric dimensions can be obtained:

$$
\begin{aligned}
&\mathrm{OA} = L = a\cos\theta + \sqrt{r^2-a^2\sin^2\theta}, q = L\sigma d\theta, \\
&\mathrm{OE} = L_1 = 2a\cos\theta - L = a\cos\theta - \sqrt{r^2-a^2\sin^2\theta}, q_1 = L_1\sigma d\theta, \\
&\angle\mathrm{COF} = \arcsin\frac{r}{a}.
\end{aligned}
\tag{26}
$$

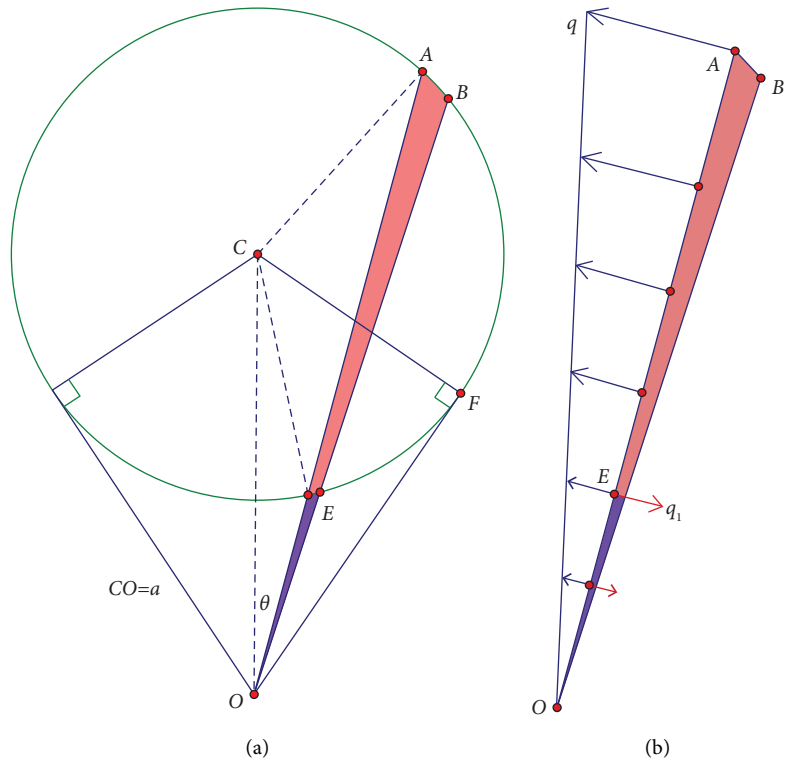

FIGURE 4: (a) Area microelements and (b) load distribution when the eccentric shaft is located outside the turntable.

2.2.1. Main Vector. The principal vector size in this case can be expressed as the difference between the equivalent concentrated forces of the two sets of linear loads.

$$\begin{aligned} df &= \frac{1}{2}qL - \frac{1}{2}q_1L_1 = \frac{\sigma}{2}L^2(\theta)d\theta - \frac{\sigma}{2}{L_1}^2(\theta)d\theta \\ &= \frac{\sigma}{2}\left[4a\cos\theta\sqrt{r^2 - a^2\sin^2\theta}\right]d\theta \\ &= 2\sigma a\cos\theta\sqrt{r^2 - a^2\sin^2\theta}\,d\theta. \end{aligned} \tag{27}$$

Therefore,

$$df_x = df\cos\theta = 2\sigma a\cos^2\theta\sqrt{r^2 - a^2\sin^2\theta}\,d\theta. \tag{28}$$

It should be noted that the integration interval in this case becomes

$$\theta \in [-\angle\mathrm{COF}, +\angle\mathrm{COF}] = \left[-\arcsin\frac{r}{a}, +\arcsin\frac{r}{a}\right]. \tag{29}$$

Combined with the left-right symmetry, the calculation result of the main vector size can be expressed as follows:

$$f_x = 4\sigma a\cdot\int_0^{\arcsin(r/a)}\cos^2\theta\sqrt{r^2 - a^2\sin^2\theta}\,d\theta. \tag{30}$$

Substituting $a = r$ into the above result, it can be found that the result is consistent with the calculation of Case 1.

2.2.2. Principal Moment. The calculation of the principal moments is similar to that of the main vectors.

$$\begin{aligned} dM &= \frac{1}{3}qL^2 - \frac{1}{3}q_1{L_1}^2 = \frac{\sigma}{3}L^3d\theta - \frac{\sigma}{3}{L_1}^3d\theta \\ &= \frac{\sigma}{3}\left[(L - L_1)\left(L^2 + LL_1 + {L_1}^2\right)\right]d\theta \\ &= \frac{\sigma}{3}\left[2\sqrt{r^2 - a^2\sin^2\theta}\left(2a^2\cos^2\theta + 2r^2 - 2a^2\sin^2\theta + a^2\cos^2\theta - r^2 + a^2\sin^2\theta\right)\right] \\ &= \frac{\sigma}{3}\left[2\sqrt{r^2 - a^2\sin^2\theta}\left(3a^2\cos^2\theta + r^2 - a^2\sin^2\theta\right)\right]d\theta. \end{aligned} \tag{31}$$

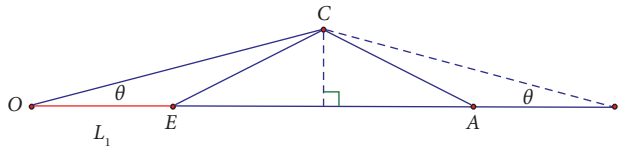

Figure 5: Geometric relationship schematic.

Combined with the left-right symmetry, it can be concluded that

$$M = \frac{4\sigma}{3}\int_0^{\arcsin(r/a)}\left[\sqrt{r^2 - a^2\sin^2\theta}\left(3a^2\cos^2\theta + r^2 - a^2\sin^2\theta\right)\right]d\theta. \tag{32}$$

In particular, when $a = r$, the results coincide with the calculation of Case 1.

$$\begin{aligned} M &= \frac{4\sigma}{3}\int_0^{(\pi/2)}\left[r\cos\theta\left(4r^2\cos^2\theta\right)\right]d\theta \\ &= \frac{16\sigma r^3}{3}\int_0^{(\pi/2)}\cos^3\theta d\theta \\ &= \frac{16mg\mu r}{3\pi}\cdot\frac{2}{3} \\ &= \frac{32mg\mu r}{9\pi}. \end{aligned} \tag{33}$$

2.3. Mathematical Model for Vibration Simulation. Based on the analysis in the previous subsection for friction, it can be concluded that the trajectory of the combined friction acting points turns out to be a circle. To be specific in the rotation-vibration system, the friction force functions as an external excitation of the oscillator shown in Figure 6.

The disc and the oscillator are connected by an eccentric shaft, while the oscillation of the eccentric shaft and the oscillator are synchronized. The dynamic equations of the oscillator in this case can be established by Newton's second law as follows:

$$\begin{cases} M\ddot{x} = -c\dot{x} - \left(K_1x + K_2x^3 + K_3x^5\right) - F_{ix}(t) + f_{sx}, \\ F_{ix}(t) = m\cdot a_{Cx}. \end{cases} \tag{34}$$

The physical meaning of all mathematical symbols in the dynamic equations is shown in Table 2.

During the vibration of the oscillator, the motion of the eccentric turntable is in the form of plane motion. Selecting the intersection point O of eccentric shaft and turntable as the base point of plane motion, it is not difficult to find that the embroil motion of the turntable is translational. From the acceleration synthesis theorem when the embroil motion is translation, the acceleration of the turntable mass center C can be expressed as follows:

$$\vec{a}_C = \vec{a}_O + \vec{a}_{CO} = \vec{a}_O + \vec{a}_{CO}^{\tau} + \vec{a}_{CO}^{n} = \vec{a}_O + CO\cdot\vec{\alpha} + \omega^2\cdot CO \overset{\alpha=0}{=} \vec{a}_O + \omega^2\cdot CO. \tag{35}$$

Project the above equation horizontally to obtain the following equation:

$$a_{cx} = \ddot{x} + \omega^2\cdot \mathrm{CO}\cos(\theta), \tag{36}$$

where $\dot{\theta} = \omega \Longrightarrow \theta = \omega t$.

Therefore,

$$\begin{aligned} &M\ddot{x} = -c\dot{x} - \left(K_1x + K_2x^3 + K_3x^5\right) - m\left[\ddot{x} + \omega^2\cdot \mathrm{CO}\cos(\omega t)\right] + f_s\sin(\omega t) \Longrightarrow \\ &(M+m)\ddot{x} + c\dot{x} + \left(K_1x + K_2x^3 + K_3x^5\right) + m\omega^2 a\cos(\omega t) - f_s\sin(\omega t) = 0 \Longrightarrow \\ &\ddot{x} + \frac{c}{M+m}\dot{x} + \frac{1}{M+m}\left(K_1x + K_2x^3 + K_3x^5\right) + \frac{m\omega^2 a}{M+m}\cos(\omega t) - \frac{f_s}{M+m}\sin(\omega t) = 0. \end{aligned} \tag{37}$$

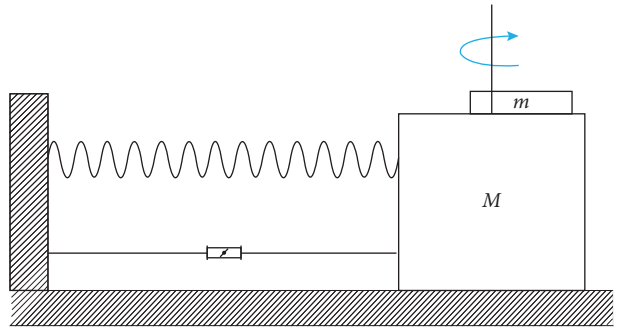

Figure 6: The simplified model of rotation-vibration system.

Table 2: Physical significance of each mathematical symbol related to the governing equations.

Mathematical symbol	Physical meaning
M	Mass of the oscillator
x	Displacement of the oscillator
c	Damping coefficient
K_i	Stiffness parameters of nonlinear spring
F_{ix}	Horizontal component force of eccentric shaft acting on the rotary table
m	Mass of the eccentric rotary table
f_{sx}	Horizontal component of friction force exerted by the eccentric rotary table on the oscillator
a_C	Acceleration of mass center of the rotary table
a_{Cx}	Horizontal component of acceleration of mass center of the rotary table
a_O	Acceleration of point O
a_{CO}	Relative acceleration of point O to centroid C
a_{CO}^{τ}	Tangential components of a_{CO}
a_{CO}^{n}	Normal components of a_{CO}
α	Angular acceleration of the turntable
ω	Angular velocity of the turntable

Assuming that

$$A = \frac{m\omega^2 a}{M+m}, B = -\frac{f_s}{M+m}, \tag{38}$$

the external excitation can be expressed as follows:

$$\frac{m\omega^2 a}{M+m}\cos(\omega t) - \frac{f_s}{M+m}\sin(\omega t) = F\cos(\omega t + \phi_0). \tag{39}$$

The expressions of amplitude F and initial phase ϕ_0 are as follows:

$$F = \sqrt{A^2 + B^2}, \phi_0 = \arctan\frac{f_s}{m\omega^2 a}. \tag{40}$$

In summary, the dimensionless equations of the oscillator can be simplified as follows:

$$\begin{cases} \dot{x} = y, \\ \dot{y} = -\mu\dot{x} - \left(k_1 x + k_2 x^3 + k_3 x^5\right) + F\cos(\omega t + \phi_0), \end{cases} \tag{41}$$

where $\mu = (c/M+m)$, $k_i = (K_i/M+m)$, and $i = 1, 2, 3$.

First, consider the structure of the autonomous system without periodic excitation, i.e., $F = 0$. The equilibrium point of the system can be represented as $E(x, y) = (x_0, 0)$, where x_0 satisfies the following equation:

$$k_1 x_0 + k_2 x_0^3 + k_3 x_0^5 = 0. \tag{42}$$

With the different parameters, the number and stability of equilibrium points will be different, resulting in the diverse phase plane structures. The numerical simulation algorithm is the fourth order Runge–Kutta method compiled in Fortran language. Origin software is applied for data plotting, including phase portraits, time histories, equilibrium branches, and bifurcation diagrams. Figure 7 shows the phase plane structure of the system under undisturbed and disturbed conditions, respectively, in the typical case of five equilibrium points.

It can be seen from Figure 7 that damping μ causes three centers $E_0, E_{\pm 2}$ of the undisturbed system to become the stable focus, while the stability of two saddle point $E_{\pm 1}$ remains unchanged after disturbance. From the phase plane structure diagram Figure 7, it is not difficult to find that damping and nonlinear spring can, respectively, change the properties and distribution structure of the system attractors while the friction information is implied in the external excitation term instead of the autonomous equations. Therefore, to study the key role of friction in the cluster oscillation, it is necessary to find out the potential friction information in the external excitation term and the influence of the external excitation frequency and amplitude on the dynamic behaviors of the system.

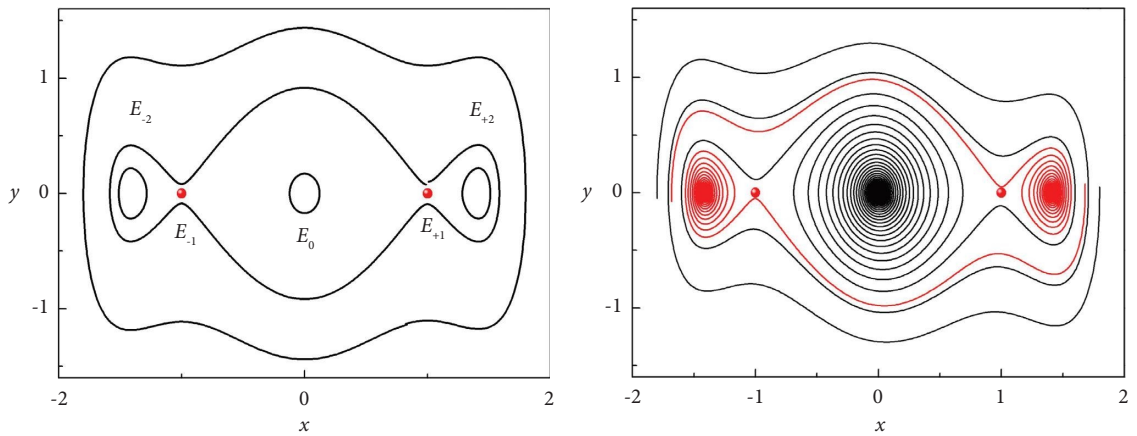

FIGURE 7: Structure on phase plane with (a) $\mu = 0.0$, $k_1 = 2.0$, $k_2 = -3.0$, and $k_3 = 1.0$ and (b) $\mu = 0.1$, $k_1 = 2.0$, $k_2 = -3.0$, and $k_3 = 1.0$.

The traditional phase portrait of trajectory Π: $\{[x(t), y(t)], t \in R\}$ reflects the relationship between different state variables in the phase space or the projection plane. Based on this idea, we can regard the slow-varying external excitation $W(t) = F\cos(\omega t + \phi_0)$ as a generalized state variable; thus, the generalized phase trajectory can be defined as Π: $\{[x(t), y(t), W(t)], t \in R\}$. The generalized phase trajectory located in the generalized phase space (x, y, W) or its projected phase plane is named transformed phase portrait (TPP), which can be used to reveal the relationship between external excitation and dynamic behaviors of the system.

3. Bursting Oscillation Mechanism with the External Excitation

The natural frequency Ω of the oscillator can be estimated using the imaginary part of the eigenvalues of E_0 in the corresponding autonomous system:

$$\Omega = \sqrt{k_1}. \tag{43}$$

Through experiments and simulations, we found that the violent oscillation of the shaking table is more likely to occur with relatively low rotary speed of eccentric rotor. The theoretical essence of this phenomenon can be described as follows: Bursting oscillation may occur with an order gap between the external excitation frequency and the natural frequency of the system.

Take the external excitation frequency $\omega = 0.005$ satisfying $\omega \ll \Omega$. Therefore, considering the whole external excitation term $W = F\cos(\omega t + \phi_0)$ as a slow variable, the control equations of system (41) can be rewritten as follows:

$$\begin{cases} \dot{x} = y, \\ \dot{y} = -\mu\dot{x} - \left(k_1 x + k_2 x^3 + k_3 x^5\right) + W, \end{cases} \tag{44}$$

which can be named as generalized autonomous system because the time variable t is not directly displayed.

3.1. Bifurcation Analysis. We can select external excitation W as the bifurcation parameter to analyze the dynamic behavior of the system. The equilibrium point of the system can be represented as $E(x, y) = (x_0, 0)$, where x_0 satisfies the following equation:

$$k_1 x_0 + k_2 x_0^3 + k_3 x_0^5 = W. \tag{45}$$

The stability of the equilibrium point is determined by the following characteristic equation:

$$\lambda^2 - \mu\lambda + \left(k_1 + 3k_2 x_0^2 + 5k_3 x_0^4\right) = 0. \tag{46}$$

In engineering practice, the damping $\mu \neq 0$. Therefore, the characteristic equation has no pure imaginary root, which indicates that Hopf bifurcation will never occur. However, the existence of a zero solution to the characteristic equation indicates that the equilibrium will undergo a fold bifurcation when the following conditions are satisfied:

$$\text{FB: } \left(k_1 + 3k_2 x_0^2 + 5k_3 x_0^4\right) = 0. \tag{47}$$

Figure 8 reflects the equilibrium points and bifurcations of the generalized autonomous system (44) under two different sets of parameters. The position of the equilibrium point is directly determined by the external excitation W. When W changes periodically with time, the trajectory of the equilibrium points in phase space is the equilibrium curve. The equilibrium curve in Figure 8(a) is divided into five segments by four fold bifurcation points $\text{FB}_{\pm1}, \text{FB}_{\pm2}$, which are, respectively, recorded as $E_0, E_{\pm1}, E_{\pm2}.E_0$ and $E_{\pm2}$ are stable focuses while $E_{\pm1}$ are unstable saddle points. The bifurcation point connects a focal point and a saddle point. This form of bifurcation is called the saddle-focus bifurcation. In Figure 8(b), the equilibrium curve is divided into three segments as $E_0, E_{\pm1}$ by fold points $B_{\pm1}$, where $E_{\pm1}$ are stable focuses while E_0 represents unstable saddle point.

When the slow-varying parameter W changes with time, a type of codimensional-1 bifurcation named saddle-focus bifurcation will occur, resulting in the jump of the

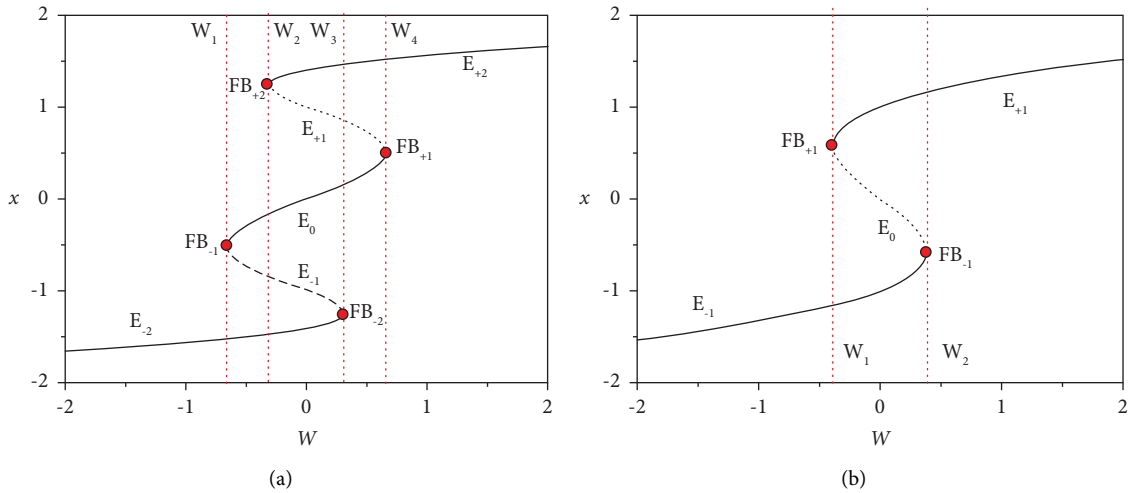

FIGURE 8: Equilibrium curves and bifurcations on plane (W, x) with (a) $\mu = 0.1$, $k_1 = 2.0$, $k_2 = -3.0$, and $k_3 = 1.0$ and (b) $\mu = 0.1$, $k_1 = -1.0$, $k_2 = 1.0$, and $k_3 = 0.0$.

equilibrium point. In other words, when the slow-varying parameter approaches the bifurcation point, the quiescent state of the fast subsystem will transit. It should be noted that the amplitude F of the external excitation W directly determines the value range of the equilibrium curve participating in the dynamic behavior of the system. Therefore, it is necessary to use numerical methods to simulate the dynamic behaviors of the oscillator under different excitation amplitudes.

It is not difficult to conclude from Figure 8 that the amplitude of the external excitation will directly determine the effective value range of the equilibrium curve. In other words, the amplitude of external excitation can indirectly affect the number and structure of equilibrium points involved in the dynamic behavior of the system. In the physical sense, the introduction of friction can increase the amplitude of the external excitation and change the oscillation structure of the shaker.

3.2. Case A. When parameters are set as $\mu = 0.1$, $k_1 = 2.0$, $k_2 = -3.0$, and $k_3 = 1.0$, the equilibrium curve of the system is shown in Figure 8(a). The numerical results show that when $F \leq 0.6564$, the system oscillates periodically with the same period as the external excitation, and there is no obvious scale effect.

However, once the amplitude $F > 0.6564$, the fold bifurcation points will participate in interference with the dynamic behavior of the system, causing the trajectory to jump between different stable equilibrium points, known as the scale effect. Figure 9 shows the phase portrait and time history in this case.

Although there are only three stable focuses in the generalized autonomous system, the stable focus E_0 will enter half-planes corresponding to $x > 0$ and $x < 0$ in turn with the change of external excitation W, causing the trajectory of the system to jump around four equilibrium points as shown in Figure 9(a). From the time history shown in Figure 9(b), it can also be seen that within a complete cycle, displacement x undergoes four oscillations, all of which exhibit a gradual decrease in amplitude and tend to an equilibrium state. According to the oscillation characteristics, the system trajectory can be divided into four spiking states $SP_{\pm1,\pm2}$ and four quiescent states $QS_{\pm1,\pm2}$, corresponding to large amplitude and small amplitude oscillations, respectively.

Comparing Figure 9 with Figure 7(b), one may find that despite of the greater amplitude of spiking state SP_{+1}, the occurrence of spiking state SP_{+2} turns out to be the key factor which directly destroys the original oscillation structure of the autonomous system. From the physical point of view, the friction acting on the eccentric turntable may cause intermittent overspeed oscillation of the shaker. To further reveal the oscillation mechanism, the transformed phase portrait and equilibrium branches of the system can be superimposed, as shown in Figure 10.

Assume the trajectory starts from P_{-1} in Figure 10, which corresponds to the minimum value $W = -0.7$. With the increase of W, the trajectory moves almost strictly along the stable equilibrium branch E_{-2}, showing the quiescent state QS_{-2}. When the trajectory reaches the bifurcation point FB_{-2}, a fold bifurcation occurs, causing the trajectory to jump towards the stable equilibrium branch E_0. Because there is a certain distance between FB_{-2} and E_0, the trajectory approaches E_0 in the form of large amplitude oscillation, appearing the spiking state SP_{+1}, and then converges to E_0, which is shown as the quiescent state QS_{+1}. Through numerical analysis, it can be found that the oscillation frequency of the spiking state SP_{+1} is approximately equal to the imaginary part of a pair of conjugate eigenvalues of the corresponding equilibrium point on E_0.

The trajectory stabilized on the equilibrium branch moves almost strictly along E_0 until it reaches the bifurcation point FB_{+1}. Then, saddle-focus bifurcation makes the trajectory jump to the stable equilibrium branch E_{+2}, presenting the spiking state SP_{+2}. When the amplitude of the

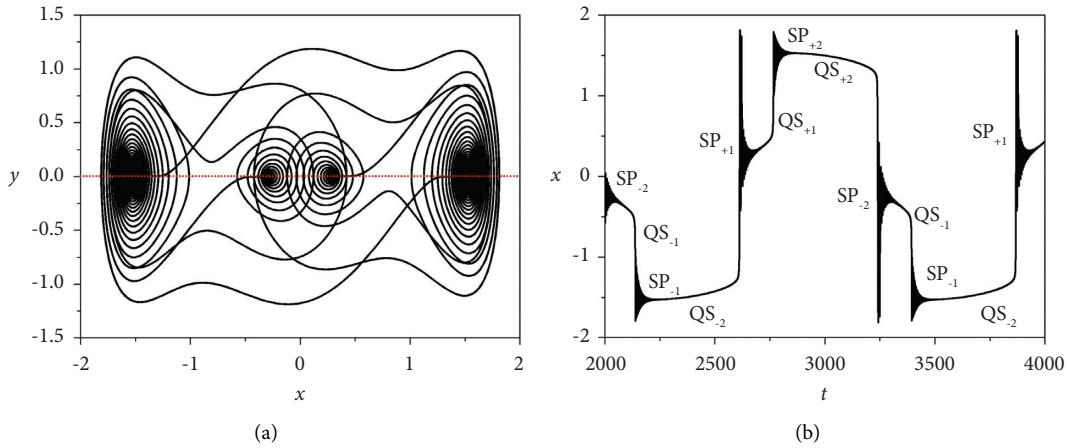

FIGURE 9: Bursting oscillations with $F = 0.70$: (a) phase portrait and (b) time history of x.

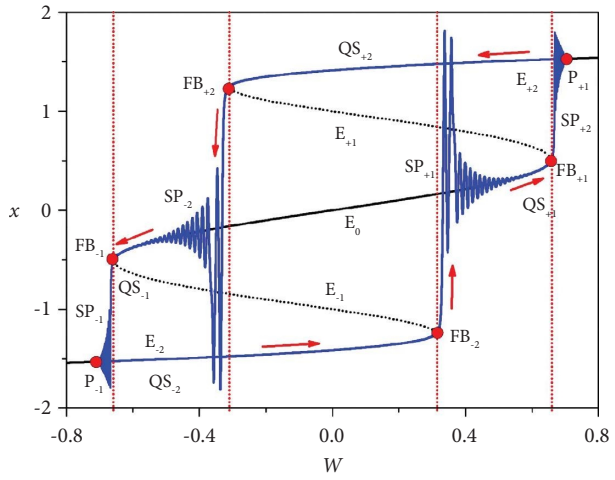

FIGURE 10: Overlap of the transformed phase portrait and equilibrium branches with $F = 0.70$.

spiking state SP_{+2} gradually decreases and finally converges to E_{+2}, the half cycle bursting oscillations is completed. The oscillation of the other half cycle has symmetry with it and will not be further elaborated.

It should be noted that the frequency of external excitation exactly equals to the angular velocity of the eccentric turntable. From the aspect of physical significance, the convergence of spiking states SP_{+1} and SP_{-2} equilibrium branch E_0 indicates that the intermittent overspeed oscillation tends to occur with the middle rotation rate. In another word, if the average change rate of external excitation $4F/(2\pi/\omega) = 2F\omega/\pi$ is relatively high, the trajectory may fail to converge to the corresponding equilibrium branch in time, thus appearing periodic oscillation with less multiple-time scale phenomena. In order to further verify this interesting conjecture, the amplitude of external excitation can be appropriately increased for simulation.

The structure of the bursting oscillation will change with the increase of the external excitation amplitude F. Figure 11 shows the dynamic behaviors of the system when $F = 2.0$. Different from the bursting behaviors when $F = 0.7$, the trajectory oscillates around only two equilibrium points. Therefore, the system motion can be divided into four parts, including two quiescent states and two spiking states, respectively. The overlap of the transformed phase portrait and equilibrium branches with $F = 2.0$ is shown in Figure 12.

Assume the trajectory starts from P_{-1} in Figure 10, which corresponds to the minimum value $W = -2.0$. With the increase of W, the trajectory moves almost strictly along the stable equilibrium branch E_{-2}, showing the quiescent state QS_{-1}. The saddle-focus fold bifurcation causes the trajectory to jump from the bifurcation point FB_{-2} to the stable equilibrium branch E_{+2}, producing spiking states SP_{-1}. After that, the oscillation amplitude of the spiking state will gradually decrease until the trajectory converges to the stable equilibrium branch E_{+2}, indicating that the half cycle bursting oscillations is completed. In terms of bifurcation mechanism, this kind of oscillation is named periodic symmetric fold/fold bursting, while from the inspect of attractor geometric structure, it can also be called point-point bursting.

Intriguingly, the system produces separated oscillation modes with different amplitudes, while the equilibrium curve and bifurcations involved are the same. The biggest

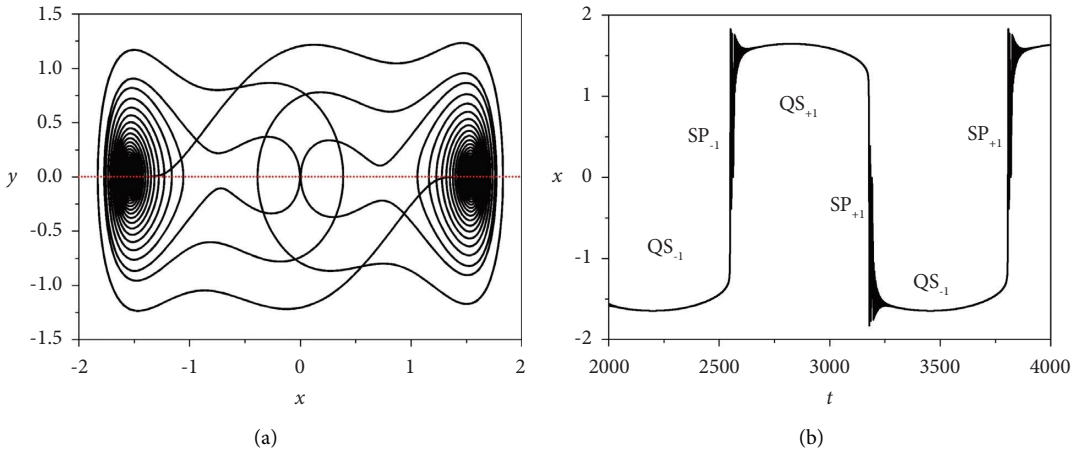

Figure 11: Bursting oscillations with $F = 2.0$: (a) phase portrait and (b) time history of x.

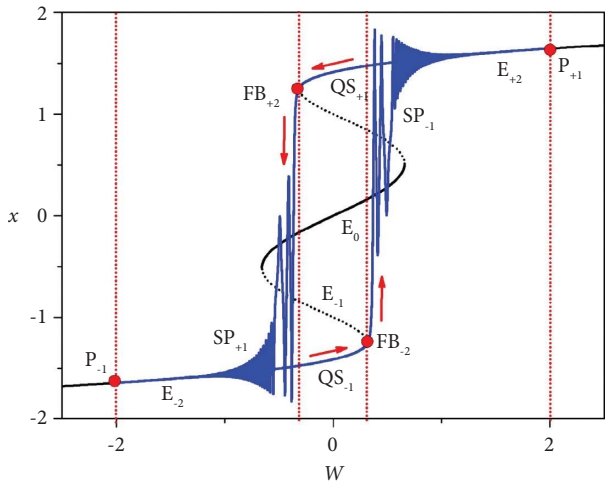

Figure 12: Overlap of the transformed phase portrait and equilibrium branches with $F = 2.0$.

difference between the two oscillation modes is whether the trajectory converges to the equilibrium branch E_0. Since the external excitation frequency remains constant, the greater amplitude implies the faster change of the external excitation. In short, when the amplitude is relatively large, the residence time of the trajectory in the attractive region of E_0 is not long enough to make it converge to the equilibrium point.

In the physical sense, this theoretical result perfectly confirms our previous conjecture proposed from Figure 10 that the intermittent overspeed oscillation tends to occur with the middle rotation rate. Besides, combining the simulation result shown in Figure 10 with formulas (38) and (40), it can be concluded that controlling the amplitude of external excitation at a high level by scaling up the rotary speed is an effective method to eliminate harmful vibrations.

3.3. Case B. Except for the way applied in case A to eliminate harmful vibrations, there is another theoretical method to avoid the occurrence of the bursting oscillations. The lower degree of nonlinearity of spring restoring force and oscillator displacement corresponds to the simpler structure of equilibrium curves. In this case, scaling down the external excitation amplitude by means of reducing the friction is also an effective method to avoid the intermittent overspeed oscillation. In specific, when parameters are set as $\mu = 0.1$, $k_1 = -1.0$, $k_2 = 1.0$, $k_3 = 0.0$, the equilibrium curve of the system is shown in Figure 8(b). It can be seen that when $F \leq 0.3850$, no bifurcation of the generalized autonomous system will occur, implying that there exists no obvious scale effect. In this case, there is a pair of coexisting periodic oscillatory attractors, respectively, around the stable equilibrium branch $E_{\pm 1}$, whose oscillation frequency is consistent with the excitation frequency. The simulation results with different initial values shown in Figure 13 confirm the coexistence of symmetrical periodic oscillations.

Based on formula (38), the reduction of the friction indicates the decrease of the amplitude as well as the invariant frequency of external excitation. The theoretical mechanism of harmful vibration elimination is that the narrower value range of equilibrium curve may involve less bifurcation, which makes the system produce simpler dynamic behaviors. From the physical point of view, it can be simply summarized that the reduction of friction at a relatively low rotating speed of the shaker can effectively eliminate the overspeed oscillation.

Once the amplitude $F > 0.3850$, the fold bifurcation points will participate in interference with the dynamic behavior of the system, causing the trajectory to jump between different stable equilibrium points, known as the scale effect. Figure 14 shows the phase portrait and time history in this case.

The existence of fold bifurcation points $\mathrm{FB}_{\pm 1}$ causes the trajectory to oscillate alternately around two equilibrium branches $E_{\pm 1}$. The trajectory can be divided into two spiking states $\mathrm{SP}_{\pm 1}$ and two quiescent states $\mathrm{QS}_{\pm 1}$. To further reveal oscillation mechanism, the overlap of transformed phase portrait and equilibrium branches is given in Figure 15.

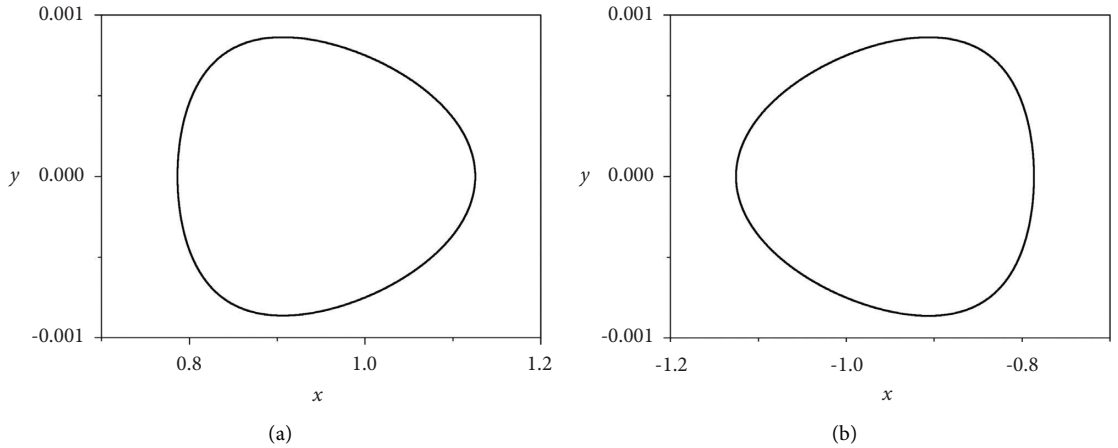

Figure 13: A pair of coexisting periodic oscillations with $F = 0.3$ and initial values (a) $(x, y) = (0.1, 0.1)$ and (b) $(x, y) = (-0.1, -0.1)$.

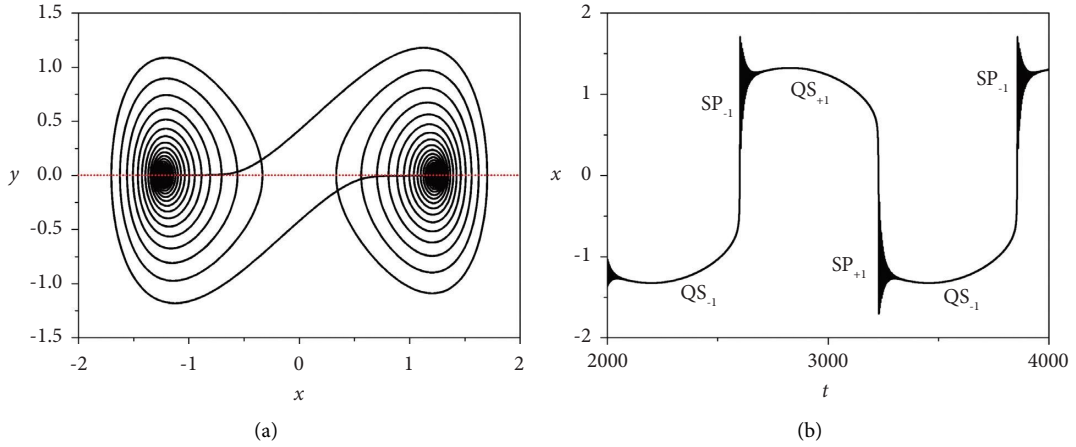

Figure 14: Bursting oscillations with $F = 1.0$: (a) phase portrait and (b) time history of x.

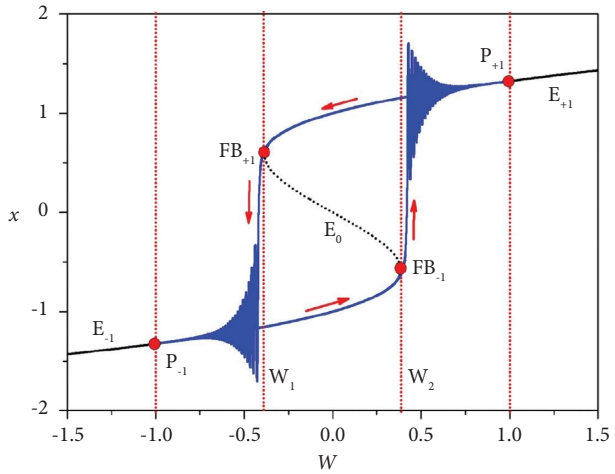

Figure 15: Overlap of the transformed phase portrait and equilibrium branches with $F = 1.0$.

Assume the trajectory starts from P_{-1} in Figure 13, which corresponds to the minimum value $W = -1.0$. With the increase of W, the trajectory moves almost strictly along the stable equilibrium branch E_{-1}, showing the quiescent state QS_{-1}. The fold bifurcation causes the trajectory to jump from the bifurcation point FB_{-1} to the stable equilibrium branch E_{+1}, producing spiking states SP_{-1}. Then, the oscillation amplitude of the spiking state will gradually decrease until the trajectory converges to the stable equilibrium branch E_{+1}, implying that the half cycle bursting oscillations are completed. Similar to the oscillation described in Figure 12, this bursting mode is named periodic symmetric fold/fold bursting or point-point bursting. If the amplitude is further increased, the equilibrium branches $E_{\pm 1}$ in the transformed phase portrait will be extended, but the topology of the attractors is going to remain unchanged.

In summary, the intermittent overspeed oscillation has a higher possibility of occurrence with the middle rotation rate. This mechanism can also be used to explain that the oscillation of washing machine is prone to occur during the speed reduction process at the end of drying. The elimination of such harmful vibration requires specific analysis. In the case of relatively high rotary speed, further increase in rotation rate is a feasible way. In the low frequency case, the reduction of friction acting on the eccentric turntable is an effective method.

4. Feasibility Analysis and Error Estimation of the Method

There are two methods for selecting the area microelement when deriving the analytic formula of the eccentric turntable friction, which, respectively, corresponds to the obtuse triangle ΔOAB and the right triangle ΔOAD shown in Figure 16. Different area selection may lead to length or area errors. Thus, it is necessary to compare the difference between the two area microelement selection methods.

4.1. Integral Error of Area. Result (48) of integrating the area differential represented by the right triangle ΔOAB is exactly equal to the area of the circle.

$$\begin{aligned}\int_0^{2\pi} \frac{1}{2} L^2(\theta) d\theta &= \frac{1}{2}\int_0^{2\pi}\left[a^2\cos^2\theta + 2a\cos\theta\sqrt{r^2 - a^2\sin^2\theta} + r^2 - a^2\sin^2\theta\right]d\theta \\ &= \pi r^2 + \frac{a^2}{2}\int_0^{2\pi}\cos 2\theta d\theta \\ &= \pi r^2 + \frac{a^2}{2}\int_0^{\pi}\cos 2\theta d2\theta \\ &= \pi r^2.\end{aligned} \tag{48}$$

We need to prove that if triangle ΔOAD is selected as the area microelement, the result of its integration is still equal to πr^2, which is equivalent to the conclusion that the integral of the triangle ΔABD area on the corresponding interval is zero. Assuming the complementary angle of ∠ACO equals to α, it should be noticed that

$$\begin{aligned}\lim_{d\theta\longrightarrow 0}\frac{S\Delta ABD}{S\Delta OAB} &= \lim_{d\theta\longrightarrow 0}\frac{(1/2)(Ld\theta)^2\tan(\alpha-\theta)}{(1/2)(Ld\theta)L - (1/2)(Ld\theta)^2\tan(\alpha-\theta)} \\ &= \lim_{d\theta\longrightarrow 0}\frac{1}{(L/(Ld\theta)\tan(\alpha-\theta)) - 1} = 0.\end{aligned} \tag{49}$$

From the sugar water inequality,

$$\min\left\{\frac{b_i}{a_i}\right\} \le \frac{b_1 + b_2 + \ldots b_n}{a_1 + a_2 + \ldots a_n} \le \max\left\{\frac{b_i}{a_i}\right\}, \quad a_i, b_i \in R^+, i \in N, \tag{50}$$

it can be concluded that

$$\min\left\{\frac{S\Delta ABD}{S\Delta OAB}\right\} \le \frac{\sum S\Delta ABD}{\sum S\Delta OAB} \le \max\left\{\frac{S\Delta ABD}{S\Delta OAB}\right\}, \tag{51}$$

where

$$\lim_{d\theta\longrightarrow 0}\min\left\{\frac{S\Delta ABD}{S\Delta OAB}\right\} = \lim_{d\theta\longrightarrow 0}\max\left\{\frac{S\Delta ABD}{S\Delta OAB}\right\} = 0. \tag{52}$$

From the squeeze theorem, it can be obtained that

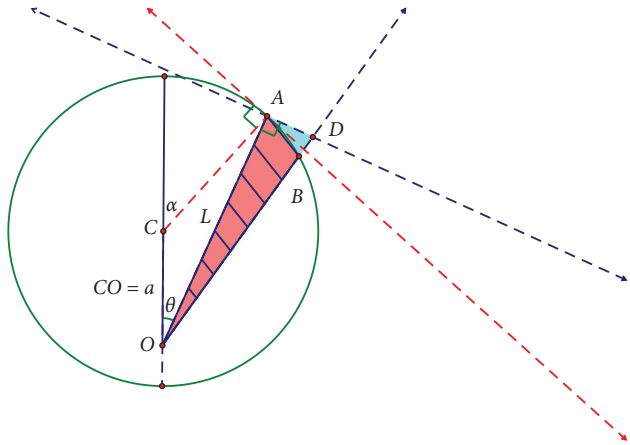

Figure 16: Area microelement ΔOAB and ΔOAD.

$$\lim_{d\theta\longrightarrow 0}\frac{\sum S\Delta ABD}{\sum S\Delta OAB}=\frac{\int_0^{2\pi}(1/2)\,(Ld\theta)^2\tan(\alpha-\theta)}{\int_0^{2\pi}(1/2)L^2d\theta-\int_0^{2\pi}(1/2)L^2\tan(\alpha-\theta)\,(d\theta)^2}=0=\frac{0}{\pi^2 r}. \tag{53}$$

Therefore,

$$\lim_{d\theta\longrightarrow 0}\sum S\Delta ABD=\int_0^{2\pi}\frac{1}{2}L^2\tan(\alpha-\theta)\,(d\theta)^2=0. \tag{54}$$

The integral of the area of ΔABD is zero, and its geometric significance is that if the integrand approaches zero on a finite integral interval, the area under its curve tends to be zero.

In the calculation process of friction, the error caused by the selection of area elements is mainly reflected in the expression of the maximum load concentration. In specific,

$$[L-L\tan(\alpha-\theta)d\theta]\sigma d\theta<q<L\sigma d\theta. \tag{55}$$

The minimum and maximum terms in this inequality correspond to the maximum load set degree when the span values are OA length and OB length, respectively. Applying the squeeze theorem, it can be proved that the integral error converges to zero by substituting these two terms into the integral calculation of friction force, which indicates that the calculation method proposed is feasible.

4.2. Integral Error of Length. Result (56) of integrating the length of the bottom edge AD is not equal to the circumference of the circle.

$$\begin{aligned}\int_0^{2\pi}L(\theta)d\theta&=\int_0^{2\pi}a\cos\theta+\sqrt{r^2-a^2\sin^2\theta}d\theta\\&=\int_0^{2\pi}\sqrt{r^2-a^2\sin^2\theta}d\theta\\&<2\pi r.\end{aligned} \tag{56}$$

When using triangle ΔOAB as an area element for integration, the area error converges to zero, while the length error cannot be ignored. The reason for this result is that when the vertex angle of the triangle ΔOAB approaches zero, the angle ∠OAB does not tend to be a right angle, but satisfies the following isometric relationship:

$$\angle\mathrm{OAB}=\frac{\pi}{2}-\angle\mathrm{BAD}=\frac{\pi}{2}-\angle\mathrm{CAO}=\frac{\pi}{2}-\alpha+\theta<\frac{\pi}{2}. \tag{57}$$

In other words,

$$\lim_{d\theta\longrightarrow 0}\alpha-\theta\neq 0. \tag{58}$$

On this basis, the error in length can be expressed as

$$\begin{aligned}\lim_{d\theta\longrightarrow 0}\frac{AB-AD}{AB}&=\lim_{d\theta\longrightarrow 0}\frac{Ld\theta[(1/\cos(\alpha-\theta))-1]}{Ld\theta\cdot(1/\cos(\alpha-\theta))}\\&=\lim_{d\theta\longrightarrow 0}1-\cos(\alpha-\theta)\neq 0.\end{aligned} \tag{59}$$

4.3. Correctness Verification in Special Case: $a\longrightarrow+\infty$. The validity of this result can be verified by taking the limit where the eccentricity tends to be infinite.

4.3.1. Main Vector

$$\begin{aligned}\lim_{a\longrightarrow+\infty}f_x&=\lim_{a\longrightarrow+\infty}4\sigma a\cdot\int_0^{\arcsin(r/a)}\cos^2\theta\sqrt{r^2-a^2\sin^2\theta}d\theta\\&=4\sigma\lim_{a\longrightarrow+\infty}\int_0^{\arcsin(r/a)}a\cos^2\theta\sqrt{r^2-a^2\sin^2\theta}d\theta.\end{aligned} \tag{60}$$

Make a vertical line of OA through the center of the circle C and intersect with OA and OB at points G and H, respectively, as shown in Figure 17. Notice that the expressions inside the integral limit integral sign have geometric significance as follows:

$$\mathrm{GH}=a\cos\theta d\theta,\ \mathrm{AG}=\sqrt{r^2-a^2\sin^2\theta}. \tag{61}$$

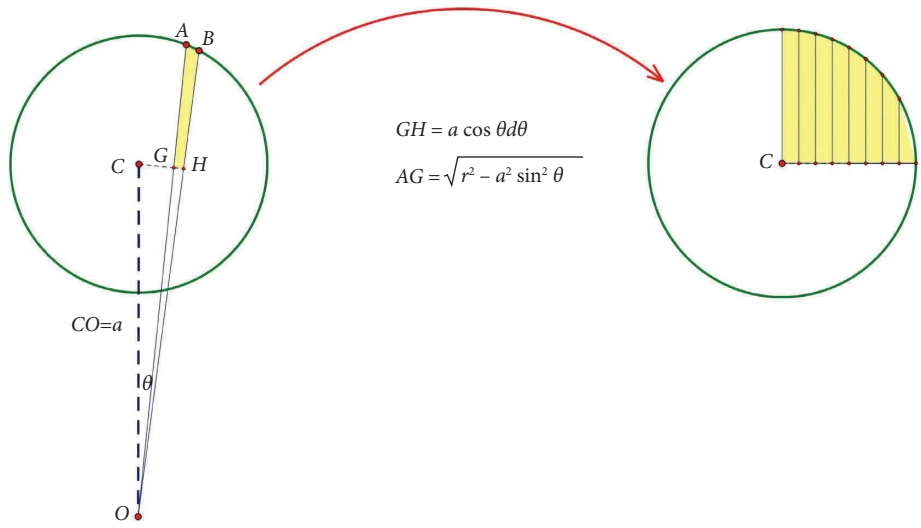

Figure 17: The geometric significance of the calculation result with $a \longrightarrow +\infty$.

Therefore, the area of quadrilateral ABGH can be expressed as

$$S_{ABGH} \approx \mathrm{GH} \times \mathrm{AB} = a\cos\theta\sqrt{r^2 - a^2\sin^2\theta}d\theta. \tag{62}$$

All the yellow microarea in the integration interval can be stitched together to form exactly a quarter circle. Based on this geometric meaning, we can derive the following integral limit:

$$\lim_{a\longrightarrow+\infty}\int_0^{\arcsin(r/a)} a\cos\theta\sqrt{r^2 - a^2\sin^2\theta}d\theta = \frac{\pi r^2}{4}. \tag{63}$$

Next, we need to prove that the following two limits of integration are equal:

$$\lim_{a\longrightarrow+\infty}\int_0^{\arcsin(r/a)} a\cos^2\theta\sqrt{r^2 - a^2\sin^2\theta}d\theta = \lim_{a\longrightarrow+\infty}\int_0^{\arcsin(r/a)} a\cos\theta\sqrt{r^2 - a^2\sin^2\theta}d\theta. \tag{64}$$

The method applied is to make a difference between these two limits of integration and prove that the limit of the difference is zero.

$$\begin{aligned}&\lim_{a\longrightarrow+\infty}\int_0^{\arcsin(r/a)} a\cos\theta\sqrt{r^2 - a^2\sin^2\theta}d\theta - \lim_{a\longrightarrow+\infty}\int_0^{\arcsin(r/a)} a\cos^2\theta\sqrt{r^2 - a^2\sin^2\theta}d\theta\\ &= \lim_{a\longrightarrow+\infty}\int_0^{\arcsin(r/a)} a\left(\cos\theta - \cos^2\theta\right)\sqrt{r^2 - a^2\sin^2\theta}d\theta.\end{aligned} \tag{65}$$

Notice that $\mathrm{CG} = a\sin\theta \le r$ is a bounded quantity; thus, the following inequality can be obtained through identity transformation:

$$0 \le a\left(\cos\theta - \cos^2\theta\right) = \frac{a\left(\cos\theta - \cos^2\theta\right)}{a\sin\theta}\cdot a\sin\theta \le \frac{a\left(\cos\theta - \cos^2\theta\right)}{a\sin\theta}\cdot r. \tag{66}$$

Besides, it is easy to know from Lopita's Law,

$$\lim_{\substack{a\longrightarrow+\infty\\ \theta\longrightarrow 0}} \frac{a\left(\cos\theta-\cos^2\theta\right)}{a\sin\theta}\cdot r = r\cdot \lim_{\substack{a\longrightarrow+\infty\\ \theta\longrightarrow 0}} \frac{-\sin\theta+2\cos\theta\sin\theta}{\cos\theta}=0. \tag{67}$$

Therefore, the following limiting expression holds from the squeeze theorem combined with the bounded quantity $\mathrm{AG}=\sqrt{r^2-a^2\sin^2\theta}$:

$$\lim_{\substack{a\longrightarrow+\infty\\ \theta\longrightarrow 0}} a\left(\cos\theta-\cos^2\theta\right)=0 \Longrightarrow \lim_{\substack{a\longrightarrow+\infty\\ \theta\longrightarrow 0}} \int_0^{\arcsin(r/a)} a\left(\cos\theta-\cos^2\theta\right)\sqrt{r^2-a^2\sin^2\theta}\,d\theta=0. \tag{68}$$

In summary, when the eccentricity distance a tends to be infinite, the main vector size of the friction is exactly

$$\begin{aligned}
&\lim_{a\longrightarrow+\infty}\int_0^{\arcsin(r/a)} a\cos^2\theta\sqrt{r^2-a^2\sin^2\theta}\,d\theta=\frac{\pi r^2}{4}\Longrightarrow\\
&\lim_{a\longrightarrow+\infty} f_x = 4\sigma\lim_{a\longrightarrow+\infty}\int_0^{\arcsin(r/a)} a\cos^2\theta\sqrt{r^2-a^2\sin^2\theta}\,d\theta\\
&=4\cdot\frac{mg\mu}{\pi r^2}\cdot\frac{\pi r^2}{4}=mg\mu,
\end{aligned} \tag{69}$$

which is completely consistent with the physical meaning of $a\longrightarrow+\infty$. In specific, $a\longrightarrow+\infty$ implies that the motion state of the turntable is instantaneous translation. According to Coulomb's law, the frictional force in this case can be obtained as $mg\mu$.

4.3.2. Principal Moments. Based on the analytical process of the main vector, the principal moment when the eccentricity distance tends to be infinite can be calculated as follows:

$$\begin{aligned}
\lim_{a\longrightarrow+\infty} M &= \lim_{a\longrightarrow+\infty}\frac{4\sigma}{3}\int_0^{\arcsin(r/a)}\left[\sqrt{r^2-a^2\sin^2\theta}\left(3a^2\cos^2\theta+r^2-a^2\sin^2\theta\right)\right]d\theta\\
&=\lim_{a\longrightarrow+\infty}\frac{4\sigma}{3}\int_0^{\arcsin(r/a)}\left[3a^2\cos^2\theta\sqrt{r^2-a^2\sin^2\theta}\right]d\theta\\
&=\lim_{a\longrightarrow+\infty}4\sigma a\cdot\int_0^{\arcsin(r/a)}\left[a\cos^2\theta\sqrt{r^2-a^2\sin^2\theta}\right]d\theta\\
&=mg\mu\cdot a\\
&=+\infty.
\end{aligned} \tag{70}$$

5. Conclusion

The distribution of friction turns out to be linear on a triangular area element with the intersection point of the eccentric shaft and the turntable plane as the vertex. The theoretical calculation results indicate that the friction between the horizontal plane and the eccentric turntable can be simplified as a combined force, with its vector direction perpendicular to the line connecting the eccentric shaft and the centroid of the turntable.

Therefore, the friction functions as an extra external excitation term in the oscillator, and the numerical value of its resultant force is positively correlated with the amplitude of the external excitation. The numerical results show that the structure of the equilibrium branches involved in the dynamic behavior of the system will change with different external excitation amplitudes.

The jumping phenomenon of the trajectory to the stable focus caused by fold bifurcation is manifested as the overspeed oscillation of the desktop medical shaker in engineering practice. From both practical and theoretical perspectives, it is found that the intermittent overspeed oscillation has a higher possibility of occurrence with the middle rotation rate. According to the bifurcation theory, the fundamental way to eliminate this harmful phenomenon without changing the internal parameters of the system is to increase the average change rate of the external excitation or simplified the attractor structure. In engineering practice, there are three methods to achieve these goals:

(1) Control the rotating speed ω of the turntable at a high level

(2) Lubricate the turntable to reduce the friction f_s in the case of low rotating speed

(3) Replace the turntable with smaller eccentricity a in the case of middle rotation rate

The three basic solutions mentioned above correspond to the situation when intermittent overspeed oscillation occurs at different working speeds, which can remedy the defects of eccentric shaft technology in practical application to a certain extent. Besides, these theoretical results also provide new ideas and perspectives for the transformation and upgrading of components with eccentric shaft, such as the eccentric turntable with adjustable eccentricity and pressure sensitive detection-feedback equipment.

6. Discussion

This paper makes some idealized assumptions and approximations such as

(1) The rotating speed ω of the turntable remains constant

(2) Friction between turntable and eccentric shaft can be ignored

(3) The oscillator vibrates only in the horizontal direction x

(4) The contact between the oscillator and the horizontal plane is smooth

(5) The diameter of the eccentric shaft is negligible relative to the size of the turntable

In engineering practice, these assumptions may not be strictly true. The circumstances with the failure of these mentioned assumptions and approximations need to be explained by more accurate and complex theoretical models, which will be carried out in our subsequent research work.

Data Availability

The data used to support the findings of this study are included within the article.

Conflicts of Interest

The authors declare that they have no conflicts of interest with respect to the research, authorship, and/or publication of this article.

Acknowledgments

This research was supported by the National Natural Science Foundation of China (Grant nos. 12072132 and 12272150) for the research, authorship, and/or publication of this article.

References

[1] Q. S. Bi, S. L. Li, J. Kurths, and Z. Zhang, "The mechanism of bursting oscillations with different codimensional bifurcations and nonlinear structures," *Nonlinear Dynamics*, vol. 85, no. 2, pp. 993–1005, 2016.

[2] S. L. Wang, J. Lu, Y. L. Zhang, K. Ge, and C. Zhong, "Analytical research on the bearing characteristics of oil film supplied with constant oil flow hydrostatic turntables under fixed eccentric load condition," *Processes*, vol. 10, no. 10, p. 2017, 2022.

[3] X. J. Han and Q. S. Bi, "Effects of amplitude modulation on mixed-mode oscillations in the forced van der Pol equation," *Nonlinear Dynamics*, vol. 111, no. 14, pp. 12921–12930, 2023.

[4] R. Qu, S. L. Li, and Q. Bi, "Forced vibration of shape memory alloy spring oscillator and the mechanism of sliding bifurcation with dry friction," *Advances in Mechanical Engineering*, vol. 11, no. 5, Article ID 1687814019851976, 2019.

[5] M. di Bernardo, C. J. Budd, A. R. Champneys et al., "Bifurcations in non-smooth dynamical systems," *Society for Industrial and Applied Mathematics Review*, vol. 50, no. 4, pp. 629–701, 2008.

[6] M. di Bernardo, C. J. Budd, and A. R. Champneys, "Grazing and border-collision in piecewise-smooth systems: a unified analytical framework," *Physical Review Letters*, vol. 86, no. 12, pp. 2553–2556, 2001.

[7] C. G. Lin, Y. N. Yang, J. L. Chu et al., "Study on nonlinear dynamic characteristics of propulsion shafting under friction contact of stern bearings," *Tribology International*, vol. 183, 2023.

[8] G. Xue, Y. J. Liu, and Y. F. Xue, "Dynamic study of the wave energy converter with inner eccentric rotor," *Journal of Tianjin University*, vol. 55, pp. 191–198, 2022.

[9] F. Wang and X. K. Ji, "Dynamic model and numerical simulation for a new eccentric rotary multiphase pump," *International Journal of Numerical Methods for Calculation and Design in Engineering*, vol. 36, no. 1, 2020.

[10] B. X. Tchomeni and A. Alugongo, "Vibrations of misaligned rotor system with hysteretic friction arising from driveshaft-stator contact under dispersed viscous fluid influences," *Applied Sciences*, vol. 11, no. 17, p. 8089, 2021.

[11] P. Glendinning, "Classification of boundary equilibrium bifurcations in planar Filippov systems," *Chaos: An Interdisciplinary Journal of Nonlinear Science*, vol. 26, no. 1, Article ID 013108, 2016.

[12] R. Qu, Y. Wang, G. Q. Wu, Z. Zhang, and Q. Bi, "Bursting oscillations and the mechanism with sliding bifurcations in a filippov dynamical system," *International Journal of Bifurcation and Chaos*, vol. 28, no. 12, Article ID 1850146, 2018.

[13] A. Colombo, M. di Bernardo, S. J. Hogan, and M. Jeffrey, "Bifurcations of piecewise smooth flows: perspectives, methodologies and open problems," *Physica D: Nonlinear Phenomena*, vol. 241, no. 22, pp. 1845–1860, 2012.

[14] R. Qu and S. L. Li, "Attractor and vector structure analyses of bursting oscillation with sliding bifurcation in Filippov systems," *Shock and Vibration*, vol. 2019, Article ID 8213808, 10 pages, 2019.

[15] M. Desroches, M. Krupa, and S. Rodrigues, "Spike-adding in parabolic bursters: the role of folded-saddle canards," *Physica D: Nonlinear Phenomena*, vol. 331, pp. 58–70, 2016.

[16] R. Prohens, A. E. Teruel, and C. Vich, "Slow-fast n-dimensional piecewise linear differential systems," *Journal of Differential Equations*, vol. 260, no. 2, pp. 1865–1892, 2016.

[17] R. Qu and S. L. Li, "Bursting oscillations and sliding motion in permanent magnet synchronous motor systems with friction factor," *Shock and Vibration*, vol. 2021, Article ID 9944286, 14 pages, 2021.

[18] Y. A. Kuznetsov, S. Rinaldi, and A. Gragnani, "One-parameter bifurcations in planar filippov systems," *International Journal of Bifurcation and chaos*, vol. 13, no. 8, pp. 2157–2188, 2003.

[19] M. K. Wei, X. J. Han, X. F. Zhang, and Q. Bi, "Bursting oscillations induced by bistable pulse-shaped explosion in a nonlinear oscillator with multiple-frequency slow excitations," *Nonlinear Dynamics*, vol. 99, no. 2, pp. 1301–1312, 2020.